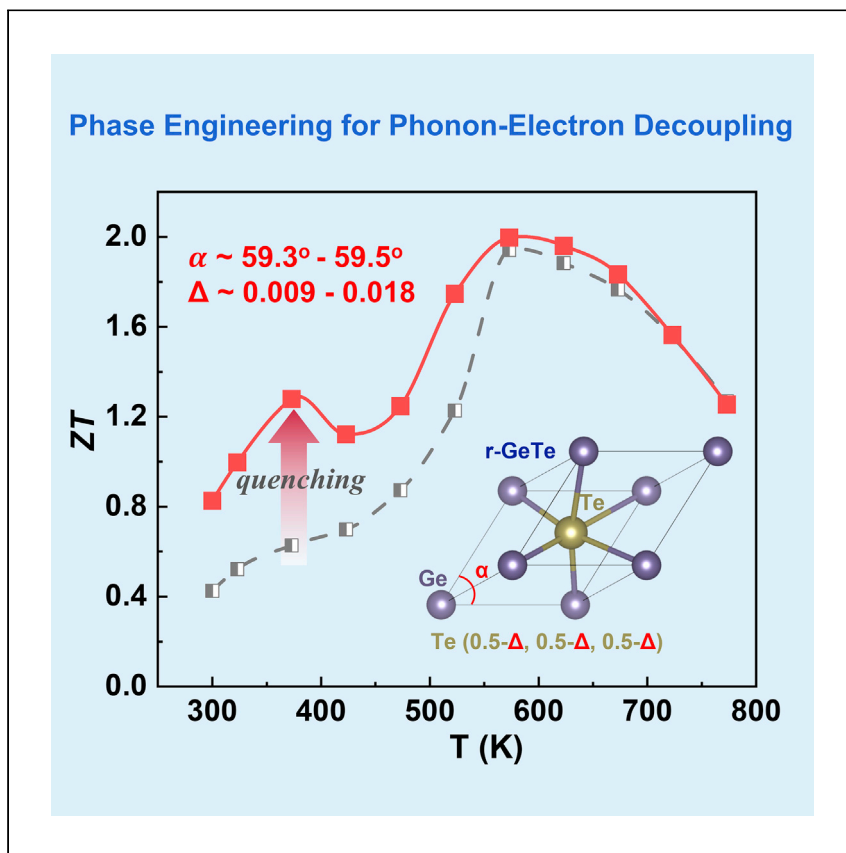**Article**

Anomalous enhancement of thermoelectric performance in GeTe with specific interaxial angle and atomic displacement synergy

Phase Engineering for Phonon-Electron Decoupling

$\alpha \sim 59.3° - 59.5°$
$\Delta \sim 0.009 - 0.018$

quenching

r-GeTe

Te

Ge α

Te $(0.5-\Delta, 0.5-\Delta, 0.5-\Delta)$

Phase engineering provides an avenue to realize phonon-electron decoupling in thermoelectric materials. Wang et al. reveal a metastable GeTe with coexisting cubic and rhombohedral phases where the rhombohedral GeTe with synergetic specific interaxial angle and atomic displacement triggers multiple-band convergence for sharply increasing the carrier mobility.

Longquan Wang, Susu Fang, Junqin Li, ..., Weigao Xu, Takao Mori, Chaohua Zhang

xuwg@nju.edu.cn (W.X.)
mori.takao@nims.go.jp (T.M.)
zhangch@szu.edu.cn (C.Z.)

Highlights

A metastable GeTe with coexisting cubic and rhombohedral phases is revealed

An r-GeTe with a specific interaxial angle and atomic displacement is extracted

Weight carrier mobility can be dramatically increased by engineering this phase

The obtained thermoelectric performance is comparable with Bi_2Te_3

CellPress
OPEN ACCESS

Article

Anomalous enhancement of thermoelectric performance in GeTe with specific interaxial angle and atomic displacement synergy

Longquan Wang,[1,3,4,5] Susu Fang,[2,5] Junqin Li,[1] Lipeng Hu,[1] Fusheng Liu,[1] Weigao Xu,[2,*] Takao Mori,[3,4,*] and Chaohua Zhang[1,6,*]

SUMMARY

Discovery and engineering of novel phase structures pave new avenues in the study of phonon-electron decoupling in thermoelectric materials, with the final aim of enhancing their figure of merit *ZT*. Here, we report a metastable GeTe phase that shows coexisting cubic and rhombohedral phases and enhances the *ZT* of GeTe-based alloys to ∼0.8 at 300 K and ∼1.3 at 373 K. This is comparable with the state-of-the-art Bi_2Te_3-based alloys in the low-temperature range. The *ZT* enhancement shows a positive correlation with an increased contribution of a special rhombohedral GeTe phase with synergetic specific interaxial angle and atomic displacement, which triggers a multiple-band convergence for enhancing carrier mobility. Moreover, quenching-induced extra phase boundaries and enhanced anharmonicity may cause extra phonon scattering that reduces the lattice thermal conductivity. This work highlights the importance of precision designing phase structures for solving the phonon-electron coupling problem in thermoelectric materials.

INTRODUCTION

Thermoelectric (TE) materials can effectively alleviate the shortage of global fossil fuels by converting waste heat into electricity directly.[1,2] The performance of a TE material is governed by a dimensionless figure of merit, $ZT = S^2\sigma T\kappa^{-1}$, where S, σ, T, and κ are the Seebeck coefficient, electrical conductivity, absolute temperature, and thermal conductivity, respectively. The κ is usually the total contribution from the lattice (κ_{lat}) and electronic (κ_{ele}) thermal conductivity.[3] The κ_{ele} is determined by the Wiedemann-Franz law $\kappa_{ele} = L\sigma T$, where L is the Lorenz number.[4] Due to the coupling effect among these electron and phonon transport parameters,[2] it is usually a challenge to enhance the *ZT* significantly. The S, σ, and κ_{lat} are the most well-known coupling parameters, showing dependence on the carrier density (n). Therefore, optimizing n is always required to maximize the power factor ($PF = S^2\sigma$) and *ZT*.[2,5] Because the phonon and electron transport share the same set of crystal lattices, effects that scatter phonons can also scatter electrons, making the κ_{ele}, carrier mobility (μ), and σ (=$ne\mu$) mutually correlated.[2] Moreover, μ is also coupled to the effective mass (m^*) that relates to S.[2] For evaluating the comprehensive effects of electron and phonon transport, the TE quality factor B is usually adopted as an important indicator of *ZT*:[5]

$$B = \left(\frac{k_B}{e}\right)^2 \frac{8\pi e(2m_e k_B T)^{3/2}}{3h^3} \cdot \frac{\mu_w}{\kappa_{lat}} T,$$

(Equation 1)

where k_B is the Boltzmann constant, h is the Planck constant, m_e is the electron mass, e is the electron charge, and μ_w is weighted mobility that combines the effects of μ

[1]College of Materials Science and Engineering, Shenzhen Key Laboratory of Special Functional Materials, Shenzhen Engineering Laboratory for Advanced Technology of Ceramics, Guangdong Research Center for Interfacial Engineering of Functional Materials, Institute of Deep Underground Sciences and Green Energy, Shenzhen University, Shenzhen 518060, P. R. China

[2]Key Laboratory of Mesoscopic Chemistry, School of Chemistry and Chemical Engineering, Nanjing University, Nanjing 210023, P. R. China

[3]International Center for Materials Nanoarchitectonics (WPI-MANA), National Institute for Materials Science (NIMS), Namiki 1-1, Tsukuba 305-0044, Japan

[4]Graduate School of Pure and Applied Sciences, University of Tsukuba, Tennodai 1-1-1, Tsukuba 305-8671, Japan

[5]These authors contributed equally

[6]Lead contact

*Correspondence: xuwg@nju.edu.cn (W.X.), mori.takao@nims.go.jp (T.M.), zhangch@szu.edu.cn (C.Z.)

https://doi.org/10.1016/j.xcrp.2022.101009

and $m^*{:}\mu_w \approx \mu(m^*/m_e)^{3/2}$.[2,5] Therefore, besides optimizing n, achieving a high ratio of μ_w/κ_{lat} for high B factor by phonon-electron decoupling is quite important for boosting ZT. Many novel strategies have been reported to enhance ZT, such as band engineering for tuning m^* and then high PF,[6,7] phonon engineering for low κ_{lat},[8–10] and interfacial engineering for synergetic optimization of PF and κ_{lat}.[11,12]

Novel mechanisms to enhance TE performance have been frequently discovered in many phase-transition materials recently.[4,13–17] S. Lee et al. reported the breakdown of the Wiedemann-Franz law in a VO_2 nanobeam with metal-insulator transition, showing very small L for anomalously low κ_{ele}.[4] L.C. Chen et al. obtained a room-temperature (RT) ZT of ~1.7 in the Cr-doped PbSe owing to a pressure-driven topological phase transition.[13] D. Byeon et al. discovered a colossal Seebeck effect in Cu_2Se near the phase-transition temperature region.[14] Many promising TE materials show noticeable phase-transition characteristics, such as GeTe,[18–20] SnSe,[21] Cu_2Se,[15,16,22] Ag_2Se,[23] and $AgBiSe_2$,[24] making phase engineering a promising pathway to decouple the transport of electrons and phonons for enhancing their ZTs. Although phase transitions could lead to a deflection of ZT value and discontinuity in the thermal expansion coefficient,[25,26] phase engineering can inspire many novel mechanisms for enhancing ZT greatly.[27]

The pristine GeTe undergoes a ferroelectric phase transition of rhombohedral $R3m$ to cubic $Fm\bar{3}m$ around ~700 K,[28] and the crystal structure of low-temperature rhombohedral GeTe (r-GeTe; having primitive-cell interaxial angle $\alpha \approx 58°$) can be considered as a slight lattice distortion along the [111] direction of the cubic GeTe (c-GeTe; $\alpha = 60°$).[29] Compared with r-GeTe, high-symmetry c-GeTe has been believed to be more favorable for obtaining high degenerate band valleys for high ZT.[18] Therefore, many efforts have been put into reducing the phase-transition temperature and increasing α toward 60° by doping or alloying with different elements, such as Mn,[28,30] Pb,[31] Sb,[32] Bi,[33] Sc,[34] Y,[35] Bi_2Te_3,[36] $AgSbSe_2$,[37] $LiSbTe_2$,[38] and $AgBiSe_2$.[9] At the same time, J. Li et al. argued that low-symmetry r-GeTe could also have superior TE performance owing to the synergetic tuning of phonon and band structures.[6] Besides α, the atomic-site displacement is another important phase parameter in GeTe, which can induce the Rashba effect as proposed by Hong et al.,[39] but specific modulation of the atomic-site displacement has not been specifically revealed yet. Quenching treatments provide a way to regulate the phase structures of GeTe for enhancing their low-temperature TE properties, as reported by Bu et al.[31] and also our previous report,[40] but the corresponding underlying mechanism is still elusive. It is worth noting that most previous reports on phase regulation are based on a single-phase model, considering $R3m$-$Fm\bar{3}m$ phase transition as a monotonic change from r-GeTe to c-GeTe,[18,28,30,41–43] but the coexistence of r-GeTe and c-GeTe has been rarely noticed.[19,44] Therefore, considering the significance of phase regulation in GeTe, precisely tuning their phase structures is still worth exploring for triggering more novel effects to enhance ZT.

In this work, we demonstrate that the synergetic precision tuning of the interaxial angle and atomic-site displacement in $(Ge_{0.87}Pb_{0.13}Te)_{0.94}(Bi_2Te_3)_{0.06}$ alloys can be realized by an appropriate quenching strategy, which leads to anomalous ZT enhancement in the low-temperature range. The ZT of our quenched GeTe-based alloys can reach ~0.8 at 300 K and 1.3 at 373 K, which is even comparable with the state-of-the-art Bi_2Te_3-based alloys in the low-temperature range. Using Raman spectroscopy, X-ray diffraction (XRD), and transmission electron microscopy (TEM), we prove the coexistence of r-GeTe and c-GeTe, where the phase boundaries can contribute extra phonon scattering for reducing κ_{lat}. The quenching strategy can increase the ratio of a novel r-GeTe phase with specific interaxial angle and atomic

Cell Reports
Physical Science
Article

CellPress
OPEN ACCESS
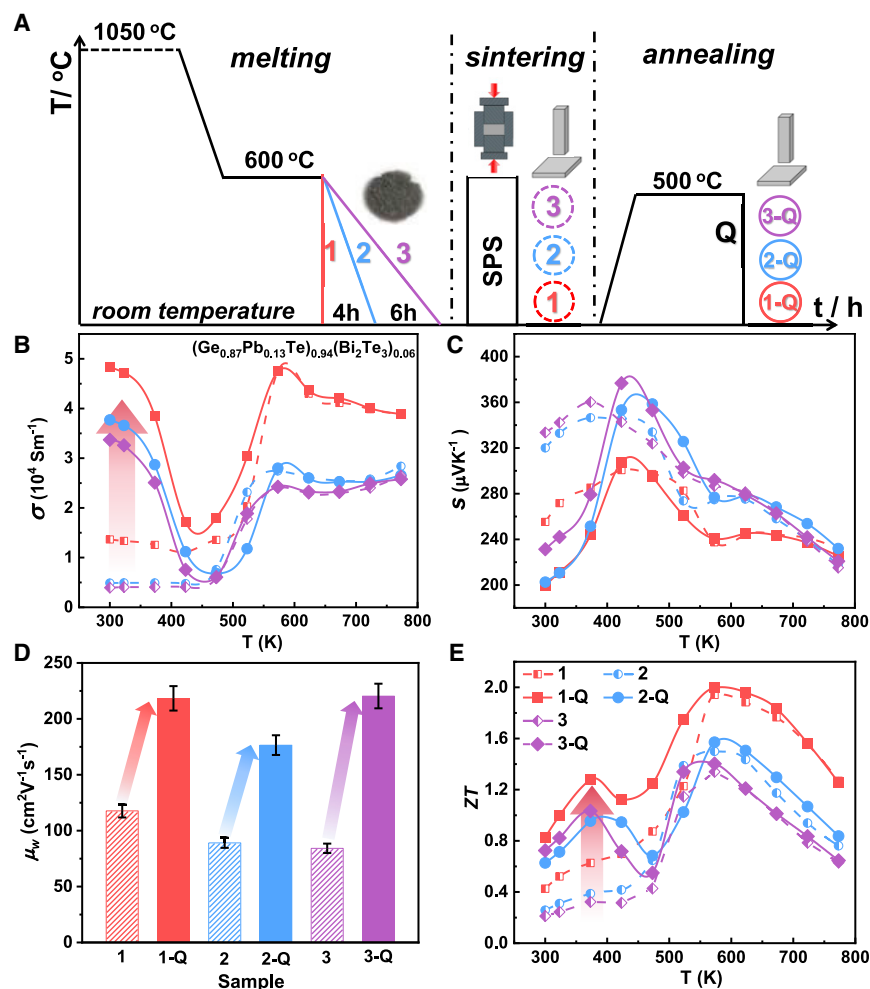
Figure 1. The anomalous *ZT*-enhancement phenomenon of GeTe-based alloys in the low-temperature range

(A) Schematic of the sample-preparation process.

(B–E) Temperature-dependent (B) electrical conductivity σ and (C) Seebeck coefficient S of the $(Ge_{0.87}Pb_{0.13}Te)_{0.94}(Bi_2Te_3)_{0.06}$ samples prepared by different processes, as well as their

(D) weighted mobility μ_w at 300 K and (E) figure of merit (*ZT*). Error bars of 5% in (D) are listed.

displacements, which increases the contribution of light valence bands for sharply enhancing the μ_w, as demonstrated by theoretical calculations.

RESULTS AND DISCUSSION

Anomalous *ZT*-enhancement phenomenon in the low-temperature range

Figure 1A illustrates the three typical steps of sample preparation: melting, spark plasma sintering (SPS), and post-annealing, which results in different $(Ge_{0.87}Pb_{0.13}Te)_{0.94}(Bi_2Te_3)_{0.06}$ samples with different treatments. Three samples after the melting process using different cooling time (quenched, 4 h, and 10 h) are sintered into bulk pellets by the SPS process, labeled as "1," "2," and "3." The SPS-derived samples 1, 2, and 3 are further treated by a post-annealing process at 500°C for 10 h and then quenched in liquid nitrogen, which are labeled as "1-Q," "2-Q," and "3-Q," respectively. The post-annealing temperature is also adjusted to prepare other samples (labeled as 1-Q/300°C, 1-Q/400°C, 1-Q/500°C, 1-Q/600°C), as displayed in Figure S1.

As shown in Figure 1B, the annealing-quenching treatment can dramatically increase the σ in the low-temperature region ($\sim$300–400 K), but the σ enhancement phenomenon almost disappears at higher temperatures (>500 K). The σ of sample 1-Q can reach 4.8×10^4 Sm^{-1} at 300 K, which is nearly three times larger than that of sample 1. On the other hand, the S decrease in the low-temperature region (300–400 K) by annealing-quenching treatment (Figure 1C) is attributed to the slight increase of n (Figure S2). Therefore, the sharp increase of σ but a small decrease of S leads to the great enhancement of PF in the quenched samples (Figure S3). As argued by M. Sist et al.,[44] the high-temperature c-GeTe possesses a higher V_{Ge} concentration than the low-temperature r-GeTe. Thus, faster cooling from high temperatures may keep more V_{Ge} in low temperatures, which can interpret the difference in n (Figure S2) and TE properties (Figure S3) for samples 1, 1-Q, 2, 2-Q, 3, and 3-Q with different cooling time after melting process, as well as samples with/without annealing-quenching treatment. Although samples 1-Q, 2-Q, and 3-Q all undergo 500°C-10 h annealing treatment, their difference in microstructures and Ge vacancies may not be fully eliminated due to the limitations of the thermodynamic phase transition and the locking diffusion process, as proposed by Tsai et al.[19]

The μ_w can be calculated based on the experimental S and σ, according to the equation proposed by G.J. Synder et al. as follows:[5]

$$\mu_w = \frac{3h^3\sigma}{8\pi e(2m_e k_B T)^{3/2}} \left[\frac{\exp\left[\frac{|S|}{k_B/e} - 2\right]}{1 + \exp\left[-5\left(\frac{|S|}{k_B/e} - 1\right)\right]} + \frac{\frac{3}{\pi^2}\frac{|S|}{k_B/e}}{1 + \exp\left[5\left(\frac{|S|}{k_B/e} - 1\right)\right]} \right].$$

(Equation 2)

As revealed in Figures 1D and S4, the sharp increase of μ_w induced by quenching treatment is the main reason for the significant increase of σ and PF in the low-temperature range. The RT μ_w of samples 1, 2, and 3 are only 118, 89, and 84 cm^{2}V^{-1}s^{-1}, respectively, but the RT μ_w of samples 1-Q, 2-Q, and 3-Q can be enhanced to 218, 176, and 220 cm^{2}V^{-1}s^{-1}, respectively, increasing by 1.85–2.62 times. Generally, higher n is not favorable for higher drift mobility μ and also weight mobility μ_w,[2,5] but the sharp increase of μ_w (Figure 1D) and μ (Figure S5) and a slight increase of n (Figure S2) can be simultaneously realized in our quenched samples. Moreover, as shown in Figure S3, the κ_{lat} in the low-temperature range (<500 K) for our quenched samples (1-Q, 2-Q, 3-Q) is even slightly lower than that of unquenched samples (1, 2, 3). Therefore, the simultaneous realization of increasing μ_w and reducing κ_{lat} for high ratio of μ_w/κ_{lat} (Figure S2) and B factor (Figure S6) may suggest a new electron-phonon-decoupling mechanism here. The RT ZT of samples 1, 2, and 3 are only 0.4, 0.22, and 0.2, respectively, but the RT ZT of samples 1-Q, 2-Q, and 3-Q can be enhanced to 0.8. 0.6, and 0.7 respectively, increasing by 2–3 times (Figure 1E).

We also observe the same anomalous ZT-enhancement phenomenon in the low-temperature range of 2–350 K as measured by a direct method (Figure S7). Although the ZT-enhancement phenomenon is nearly independent of the melting process (Figure 1E), it shows great dependence on the annealing-quenching process (Figure S8). The anomaly disappears at the lower post-annealing temperature of 300°C (Figure S8), which should be attributed to the absence of the specific metastable phase structure discussed below. The ZT-enhancement phenomenon disappears at higher temperatures >473 K (Figure 1E) and also disappears after the first-round TE test (Figure S9), indicating a metastable microstructure for inducing these novel properties. It is worth noting that the ZT-enhancement phenomenon

CellPress
OPEN ACCESS
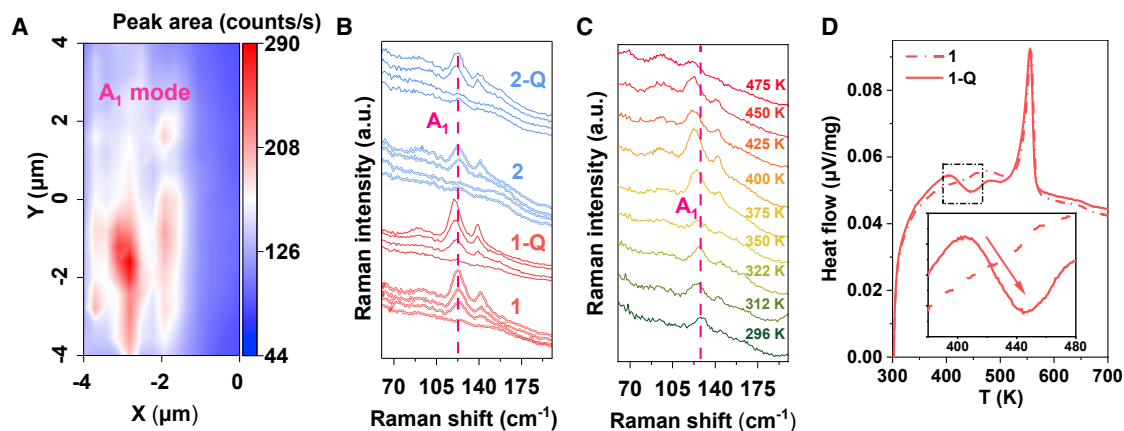
Figure 2. The metastable GeTe with coexisting rhombohedral and cubic phases
(A) The A_1-mode Raman mapping image at room temperature for sample 2-Q.
(B) Raman spectra at random sites of samples 1, 1-Q, 2, and 2-Q, and the red dashed lines highlight the position of the A_1 mode for rhombohedral GeTe (r-GeTe).
(C) Temperature-dependent Raman spectra for sample 2-Q, and the A_1 mode is highlighted.
(D) Differential scanning calorimetric (DSC) characterization for samples with (1-Q) and without (1) quenching. The sample 1-Q has slight exothermic peaks near 400–480 K, as shown in the inset of (D).

can be recovered by performing the annealing-quenching treatment again on the samples after the first-round TE test (Figure S9). As shown in Figure S10, the ZT-enhancement phenomenon is repeatable when keeping the testing temperature in the low-temperature range (<373 K), indicating the applicability of this anomalous ZT enhancement for low-temperature TE applications.

Metastable GeTe with coexisting rhombohedral and cubic phases

As shown in Figure 2A–2C, we conduct Raman measurements to understand the "structure-property" relation for the anomalous ZT-enhancement phenomenon. The Raman features are quite sensitive to the phase structure of GeTe, which can be used to distinguish the c-GeTe and r-GeTe.[45,46] The r-GeTe shows representative peaks around 120 (A_1 mode) and 140 cm^{-1} (spurious oxide mode), while the c-GeTe shows nearly no Raman peaks.[45,46] The Raman signals at random sites of the samples 1, 2, 1-Q, and 2-Q (Figure 2B) indicate that each sample can have Raman-sensitive r-GeTe phase in some regions but Raman-silent c-GeTe phase in other regions, demonstrating the coexistence of r-GeTe and c-GeTe phases in each sample. Figure 2A displays an A_1-mode Raman mapping image at RT for sample 2-Q in a region of 4 × 8 μm, further demonstrating the random distribution of the coexisted r-GeTe and c-GeTe phases in one sample.

To understand the temperature-dependent ZT-enhancement phenomenon (Figure 1E), we also conduct the temperature-dependent Raman measurements on a Raman-sensitive r-GeTe region for sample 2-Q in the temperature range of 296–475 K (Figure 2C). The A_1 Raman mode in sample 2-Q gradually softens (decreases to lower Raman shift) and broadens with increasing temperature, which should be ascribed to the lattice expansion and increasing anharmonicity.[45] As revealed by Bellin et al.,[45] the A_1 Raman mode in pristine GeTe gradually weakens and broadens with temperature, which is interpreted by the high propensity of GeTe to form V_{Ge} during the phase transition $R3m$-$Fm\bar{3}m$. However, the A_1 Raman mode in our sample 2-Q shows more anomalous behavior (Figure 2C), which is weaker below 350 K, stronger between 375 K and 450 K, and weaker again above 475 K. Comparing our results with that of pristine GeTe by C. Bellin et al.,[45] we infer that the r-GeTe

CellPress
OPEN ACCESS

phase in our quenched samples is metastable in the low-temperature range (<375 K) and turns to the normal state again above 375 K, which agrees well with the temperature-dependent change tendency of σ (Figure 1B).

The above hypothesis of metastable structures can be further proved by the differential scanning calorimetric (DSC) measurement (Figure 2D). Samples 1 and 1-Q (Figure 2D), as well as samples 2 and 2-Q (Figure S11), all have obvious endothermic peaks around 550 K that are related to the normal $R3m$-$Fm\overline{3}m$ phase transition in GeTe. Although the quenching treatment does not change the phase-transition temperature, quenched samples (1-Q, 2-Q) show small exothermic peaks around 400–480 K (inset of Figures 2D and S11), in keeping with the temperature range in which the anomalous ZT-enhancement phenomenon begins to disappear (Figure 1E). Therefore, as we inferred, the high-energy metastable structures shift to low-energy stable structures with temperature increasing, which leads to the release of thermal energy and the disappearance of metastable structures. Thus, the Raman and DSC prove that our quenched GeTe-based alloys have metastable microstructures in the low-temperature range with the coexistence of c-GeTe and r-GeTe phases, which accounts for the anomalous ZT-enhancement phenomenon in the low-temperature range.

Microstructural characterization by TEM

TEM is frequently employed to analyze the nano and microstructures of TE materials.[47] As revealed by previous reports,[11,48,49] the r-GeTe usually displays the signature of herringbone domain structures, showing altering dark-white contrast in the low-magnification TEM images, while the c-GeTe does not. The formation of herringbone structures in GeTe is usually attributed to the complex interaction between strain and electrostatic interaction during the phase transition from the high-temperature centrosymmetric phase to the low-temperature non-centrosymmetric phase.[11] In the low-magnification TEM image of the 1-Q sample (Figure 3A and S12), the herringbone structures can be found in some regions but not in others, also suggesting the coexistence of r-GeTe and c-GeTe phases. Moreover, planar V_{Ge} or named stacking faults have also been widely observed in the GeTe-based alloys,[8,11,36] which can also be observed in our quenched samples (Figure 3B) and our previous reports as well.[36,40] A boundary region between the c-GeTe and r-GeTe is also examined in TEM (Figure 3C), where a thin transition layer can be identified. The corresponding fast Fourier transform (FFT) and inverse FFT analysis on the marked two regions in Figure 3C further demonstrate the coexisting rhombohedral (Figures 3D–3E) and cubic phases (Figures 3F–3G) qualitatively, though the measurement error of angles (~1–2%) needs to be considered.

Phase-structure-evolution characterization by XRD

To further reveal the sample structures from a macroscopic view, we measure the XRD patterns of the samples without (1, 2, 3) and with (1-Q, 2-Q, 3-Q) the annealing-quenching treatment, as shown in Figure 4. The c-GeTe (PDF#52–0849) and r-GeTe (PDF#47–1079) show an obvious difference in the secondary stronger XRD peaks around 42° (Figure 4A), which are frequently used to distinguish the r-GeTe and c-GeTe.[19,30,41,44] Around 42°, the r-GeTe has two representative peaks of (024) and (220), while the c-GeTe only has a single (220) peak. Compared with unquenched samples (1, 2, 3), those quenched samples (1-Q, 2-Q, 3-Q) have very obvious splitting peaks around 42°, indicating a more obvious rhombohedral phase after the quenching treatment. The unquenched samples (1, 2, 3) tend to have single peaks around 42° but also show a broader shoulder that indicates the continued existence of rhombohedral phases.

Cell Reports
# Physical Science
Article

CellPress
OPEN ACCESS
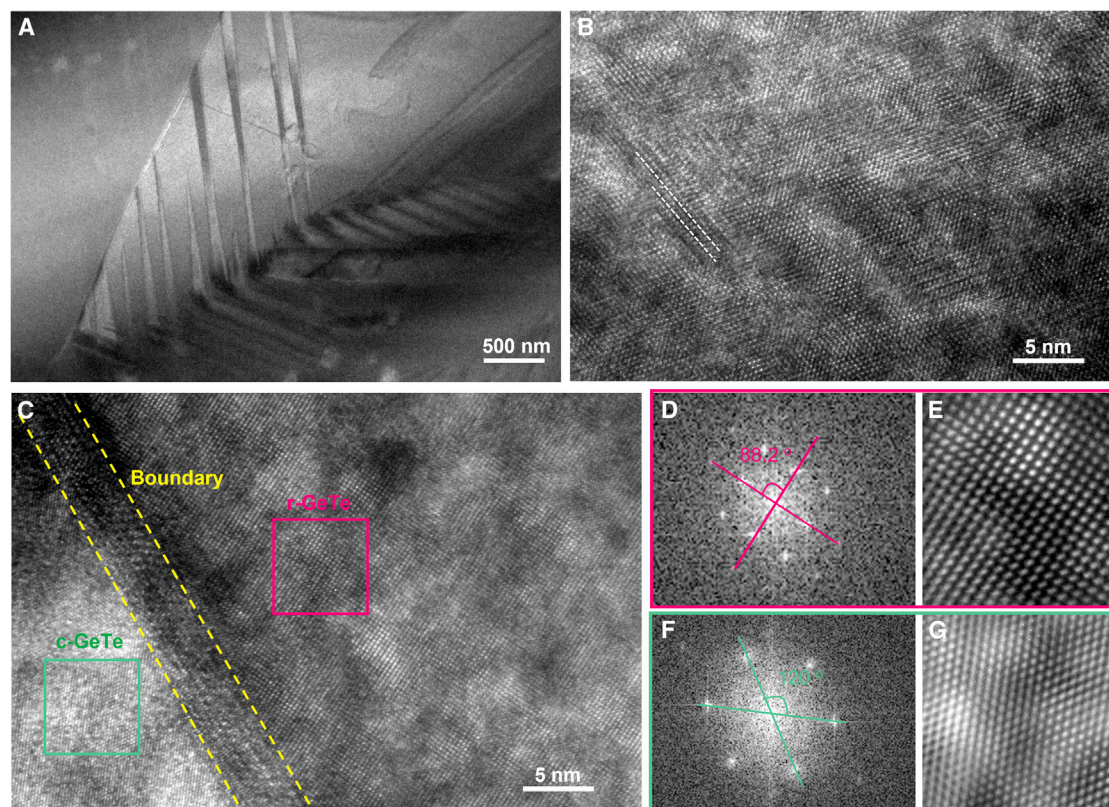
Figure 3. Microstructural characterizations by transmission electron microscopy (TEM)
(A) A typical TEM image of a region with herringbone structures.
(B) High-resolution TEM (HRTEM) image showing planar defects.
(C) HRTEM image showing a boundary region.
(D and E) Fast Fourier transform (FFT) and inverse FFT images for the marked red region in (C).
(F and G) FFT and inverse FFT images for the marked green region in (C). The representative sample 1-Q is used for the TEM test.

To quantitatively distinguish the c-GeTe and r-GeTe phases, we perform the Rietveld refinement on those XRD patterns using a two-phase model that uses primitive cells of c-GeTe and r-GeTe (Figure 4B). We also perform the XRD refinement using a frequently used single-phase mode, which, however, shows poorer refinement-goodness factors (R_p, R_{wp}) than the two-phase model (Tables S1 and S2). Based on the general structure of r-GeTe and c-GeTe,[39] the Ge atomic site is set as (0, 0, 0), and the Te atomic site is set as (0.5-Δ, 0.5-Δ, 0.5-Δ), where the off-center atomic displacement (Δ) of c-GeTe is fixed as 0, and the Δ of r-GeTe is fitted here. Moreover, the interaxial angle (α) of c-GeTe is fixed at 60°, and the α of r-GeTe is fitted here. As highlighted in Figure 4C, the XRD pattern of sample 1-Q around 42° can be well fitted by the mixed rhombohedral and cubic phases. After Rietveld refinement, the derived proportion of c-GeTe and r-GeTe is shown in Figure 4D, and the fitted α and Δ of the r-GeTe phase are displayed in Figures 4E and Tables S1 and S3. Therefore, the annealing-quenching process tends to have the following three effects. First, it reduces the proportion of c-GeTe below 50% but significantly increases the proportion of r-GeTe, exceeding 50% (Figure 4D). Second, it increases the α of the r-GeTe from ~58.9° to 59.1° to the narrow range of ~59.3°–59.5°. Third, it decreases the Δ of the r-GeTe from ~0.027 to 0.030 to the range of ~0.010–0.018, suggesting the weakening of ferroelectricity. These quenching-induced effects should be ascribed to the incomplete relaxation during the quenching process, resulting

CellPress
OPEN ACCESS

Cell Reports
Physical Science
Article
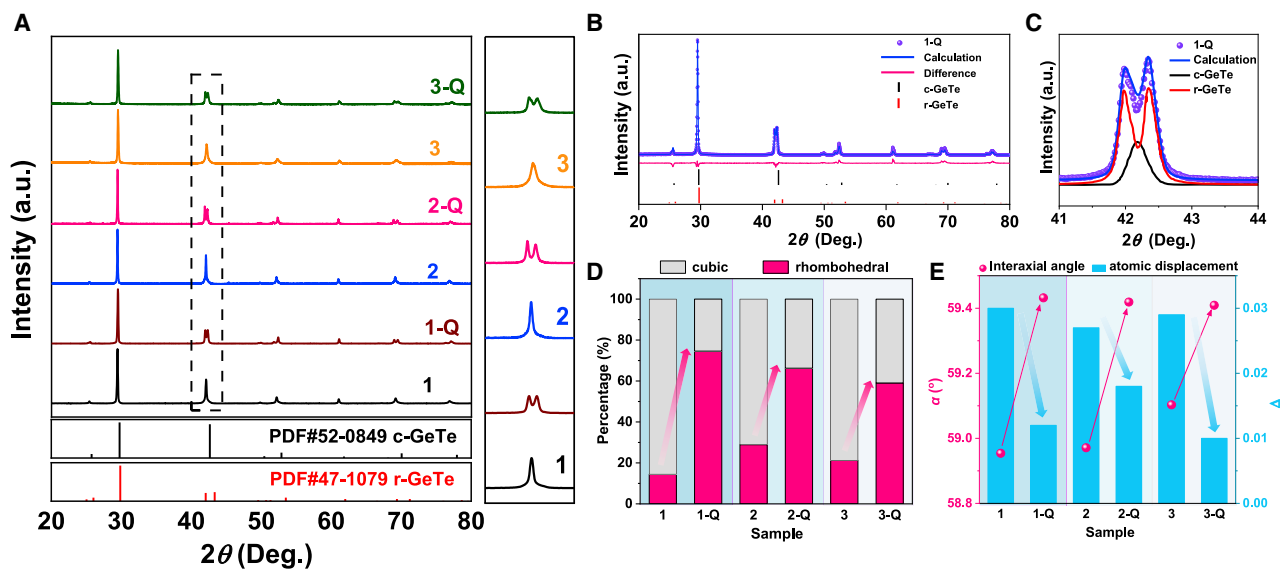
Figure 4. Phase-structure-evolution characterizations by X-ray diffraction (XRD)

(A) XRD patterns of the $(Ge_{0.87}Pb_{0.13}Te)_{0.94}(Bi_2Te_3)_{0.06}$ samples prepared by different processes. The characteristic XRD peaks around 42° are magnified on the right of (A).

(B) Rietveld refinement analysis from the XRD pattern of a 1-Q sample using two phases of cubic GeTe (c-GeTe) and r-GeTe.

(C) The Rietveld refinements around 42° in (B) are magnified.

(D) The fitted phase percentage of c-GeTe and r-GeTe.

(E) The interaxial angle (α) and atomic displacement (Δ) for the fitted r-GeTe phase.

in a metastable r-GeTe with α and Δ that lie between the c-GeTe and the stable r-GeTe.

We also performed XRD Rietveld refinement on the samples with different post-annealing temperatures (Figure S13; Tables S1 and S3). For the samples of 1-Q/400°C, 1-Q/500°C, and 1-Q/600°C showing the phenomenon of anomalous ZT enhancement, the fitted r-GeTe phase shows increased percentage, increased α in the range of ~59.3°–59.5°, and decreased Δ in the range of ~0.009–0.015 (Figure S13). However, for the 1-Q/300°C sample showing no ZT-enhancement phenomenon, the fitted r-GeTe phase nearly shows no difference from the unquenched sample 1 (Figure S13). Furthermore, we also perform the Rietveld refinement analysis on the XRD patterns of the $(Ge_{0.87}Pb_{0.13}Te)_{1-x}(Bi_2Te_3)_x$ alloys (x = 1%, 3%, 5%, 7%) with and without annealing-quenching treatment, as shown in Figure S14. Our previous work has revealed that the anomalous phenomenon can only show up in the samples with higher Bi_2Te_3 composition (x = 5%, 7%) after quenching treatment,[40] which shows a great connection with the r-GeTe phase with higher α of ~59.5° (Figure S14). On the other hand, the samples with lower Bi_2Te_3 composition (x = 1%, 3%) are dominated by the r-GeTe phase (>90%) but with lower α (<59°), and the annealing-quenching treatment cannot result in anomalous ZT-enhancement phenomenon in these samples.[40] Therefore, all these pieces of evidence indicate that the quenching-induced r-GeTe phase with synergetic specific α (~59.3°–59.5°) and Δ (~0.009–0.018) have great connection with the anomalous ZT-enhancement phenomenon.

Band structure modulation by tuning the interaxial angle and atomic displacement

As shown in Figure 5, we further perform density functional theory (DFT) calculations to understand the mechanism underneath the anomalous ZT-enhancement

CellPress
OPEN ACCESS
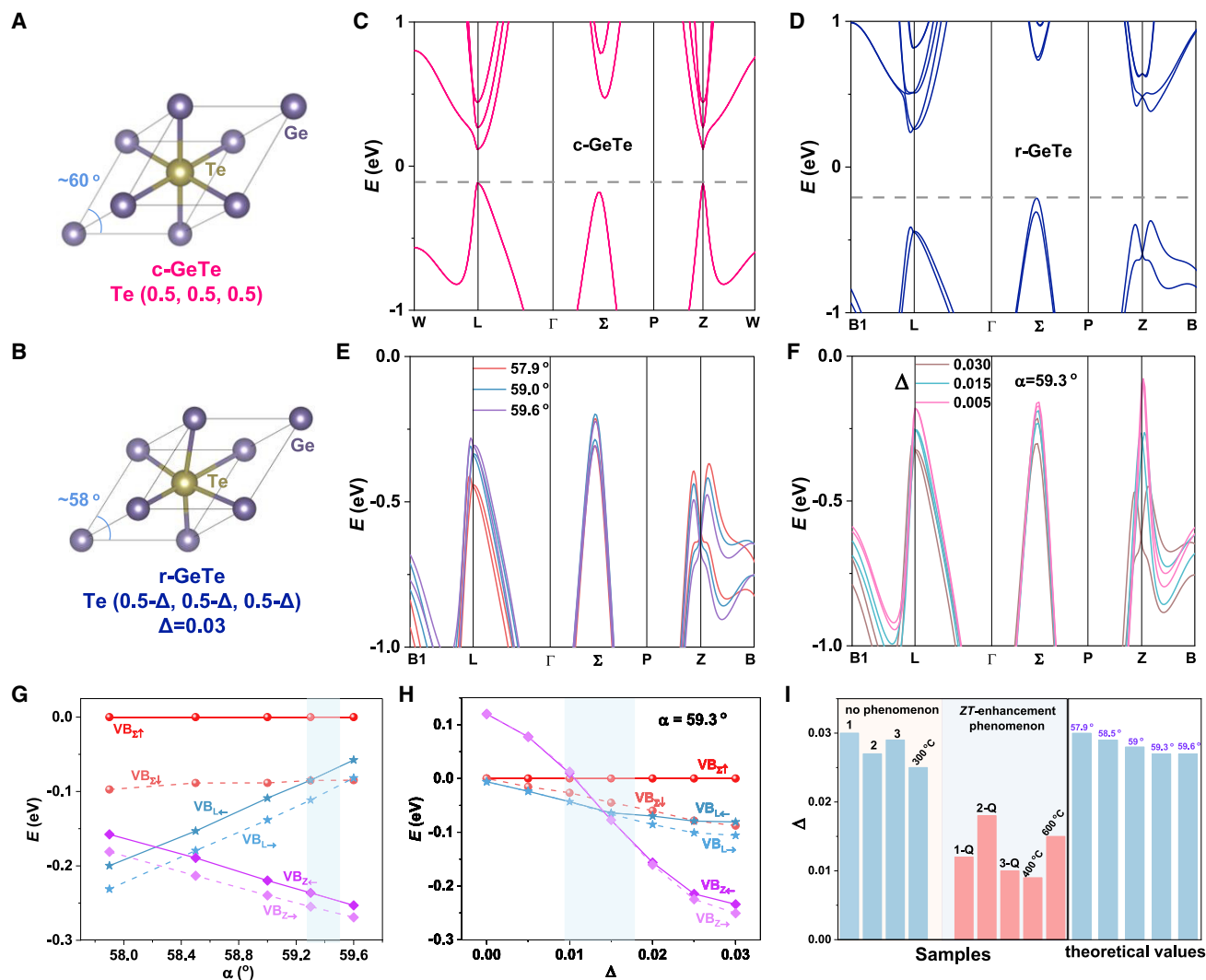
Figure 5. Band-structure modulation by tuning the interaxial angle and atomic displacement

(A and B) The primitive cell of (A) c-GeTe and (B) r-GeTe, showing the difference in the interaxial angle (α) and off-center atomic displacement (Δ).

(C and D) Calculated band structures for (C) c-GeTe and (D) r-GeTe.

(E and F) The evolution of valence-band edges by tuning the (E) α, and (F) Δ.

(G and H) The evolution of valence-band energy at L, Σ, and Z points by tuning the (G) α and (H) Δ. The shadow region highlights the experimental α and the Δ derived from the XRD Rietveld refinement.

(I) The Δ of the experimental samples with and without anomalous ZT-enhancement phenomenon. The theoretical Δ values after relaxation for the r-GeTe with different α are also listed for comparison.

phenomenon induced by the metastable r-GeTe phase with specific α and Δ. The DFT calculations are based on the primitive cell of GeTe, where the crystal structures of c-GeTe and r-GeTe are depicted in Figures 5A and 5B, respectively. Figures 5C and 5D show the band structures of c-GeTe and r-GeTe, respectively. The highest energy valence bands locate at L and Z points for the c-GeTe (Figure 5C) but at Σ point for the r-GeTe (Figure 5D). Moreover, the offset energy of $L(Z)$ and Σ in c-GeTe is much smaller than that in r-GeTe (Figures 5C–5D), indicating higher energy convergence in c-GeTe for higher TE performance. Different from the c-GeTe, the r-GeTe shows obvious valence-band-splitting behaviors at Σ, L, and Z points, which is owing to the atomic-displacement-induced Rashba effect.[39] The splitting valence bands at Σ, L, and Z points are labeled as $VB_{\Sigma\uparrow}$ and $VB_{\Sigma\downarrow}$, $VB_{L\rightarrow}$ and $VB_{L\leftarrow}$, and

$VB_{Z\rightarrow}$ and $VB_{Z\leftarrow}$, respectively, where the subscripts of ↑ ↓ represent subbands at a higher and lower energy level, and the subscripts of → ← represent the subbands at the right and left side of the $L(Z)$.

Figure 5E displays the evolution of band structures by tuning the α, where the Δ is relaxed to the energy-stable state. When α increases approach 60°, compared with the VB_Σ, the VB_L bands lift, but the VB_Z bands decline. Figure 5F displays the evolution of band structure by tuning the Δ, where the α is fixed at 59.3°. When the Δ decreases from 0.03 to 0, the VB_L bands and VB_Z bands all lift toward the VB_Σ bands, and the band-splitting effect is gradually weakened. Figures 5G and 5H summarize the evolution of band energy by tuning the α and the Δ, respectively, where the $VB_{\Sigma\uparrow}$ energy is set as 0 eV. The shadow region in Figures 5G and 5H also highlight the experimental α and the Δ derived from the XRD Rietveld refinement. The increase of α is efficient for reducing the offset energy between VB_L and VB_Σ (Figure 5G), reaching optimal α around 59.3°. However, the increase of α can increase the offset energy between VB_Z and VB_Σ. At fixed α = 59.3°, further decreasing the Δ can facilitate the convergence of all these multiple valence-band edges, reaching optimal Δ around 0.0.010–0.015. Therefore, for the quenching-induced r-GeTe phase with synergetic specific α (~59.3°–59.5°) and Δ (~0.009–0.018), the contribution of the light valence bands of VB_L and VB_Z is greatly enhanced, leading to the sharp increase of μ_w for high ZT. It is also worth noting that theoretical Δ values of those r-GeTe with different α after structural relaxation are close to those unquenched samples (Figure 5I), indicating that the quenched samples with specific Δ should be in the non-equilibrium metastable state.

Discussion on other influencing factors

Besides the sharp increase of μ_w, the decrease of κ_{lat} (Figure S3) after annealing-quenching treatment is also worth discussing here. As discussed in our previous work,[36] Pb and Bi_2Te_3 alloying can introduce various phonon scatterings from point defects, grain boundaries, and stacking faults, which lead to a low κ_{lat} of 0.56 $Wm^{-1}K^{-1}$ at 300 K for our sample 1. Further annealing-quenching treatment can reduce the κ_{lat} of sample 1-Q to 0.46 $Wm^{-1}K^{-1}$ at 300 K (Figure S15). As demonstrated from the above structural characterizations, the quenching-induced metastable structure with coexisting r-GeTe and c-GeTe phases can bring in extra phase boundaries, which induce extra phonon scatterings for decreasing κ_{lat}. On the other hand, the metastable r-GeTe phase with specific α and Δ may lead to deviation of the harmonic relationship between the force and atomic displacement, which enhances the anharmonicity for decreasing κ_{lat}.[50] These effects inducing the difference between sample 1 and 1-Q in κ_{lat} are further demonstrated by corresponding theoretical modeling (Figure S15). Though extra defects for scattering phonons may also scatter charge carriers more or less, a sharp net increase of μ_w/κ_{lat} for high ZT can still be realized here owing to the dominant increase of μ_w from the increased contribution of light valence bands.

Based on the XRD, DSC, and TE results, we further discuss the influencing factors that trigger the anomalous ZT-enhancement phenomenon. To realize the quenching-induced anomaly, as demonstrated by the Bi_2Te_3 alloying effects in $(Ge_{0.87}Pb_{0.13}Te)_{1-x}(Bi_2Te_3)_x$ (Figure S14), higher Bi_2Te_3 content is required to boost the α of the r-GeTe phase before quenching to ~59°. For example, the un-doped GeTe only shows α ~58° and then does not show the anomalous ZT-enhancement phenomenon (Figure S16). The Pb-free sample of $(GeTe)_{0.93}(Bi_2Te_3)_{0.07}$ also has α of ~59° before quenching and then displays the anomalous ZT enhancement (Figures S17–S19), even though its near-RT ZT is a bit lower than those Pb-alloyed samples (Figure S20). Moreover, the

Cell Reports
Physical Science
Article

CellPress
OPEN ACCESS

realization of specific α and Δ synergy should have great connection with the phase transition in GeTe. Although the PbTe, SnTe, and GeTe are the same group IV–VI chalcogenides,[51,52] only the GeTe has the $R3m\text{-}Fm\overline{3}m$ phase transition, while the PbTe and SnTe keep the cubic structures above RT. As shown in Figures S17–S19, upon annealing-quenching treatment, only the $(GeTe)_{0.93}(Bi_2Te_3)_{0.07}$ show the anomalous phenomenon of enhanced μ_w and ZT, while the $(SnTe)_{0.93}(Bi_2Te_3)_{0.07}$ and $(PbTe)_{0.93}(Bi_2Te_3)_{0.07}$ show depressed μ_w and σ (Figure S18). The corresponding XRD patterns (Figure S19) further confirm the key role of the quenching-induced r-GeTe phase in $(GeTe)_{0.93}(Bi_2Te_3)_{0.07}$ for the anomalous phenomenon, while the annealing-quenching treatment cannot induce anomalous phenomenon in the single cubic $(SnTe)_{0.93}(Bi_2Te_3)_{0.07}$ and $(PbTe)_{0.93}(Bi_2Te_3)_{0.07}$ without phase transition. Moreover, as demonstrated by Figure S13, to obtain specific α and Δ synergy, the annealing-quenching temperature should be higher than the phase-transition temperature. Therefore, as summarized in Figure S21, to obtain specific α and Δ synergy for the anomalous ZT-enhancement phenomenon, two premises seem to be required: one is to increase the α of r-GeTe phase to $\sim$59° before quenching, and the second is quenching above the phase-transition temperature.

In summary, we build a bridge between the anomalous ZT-enhancement phenomenon in quenched GeTe-based alloys and a metastable structure that show coexisting c-GeTe (α = 60°) and the novel r-GeTe with synergetic specific interaxial angle (α = 59.3°–59.5°) and atomic displacement (Δ = 0.009–0.018), as demonstrated by the Raman, XRD, TEM, DSC, and DFT results. The ZT values of our $(Ge_{0.87}Pb_{0.13}Te)_{0.94}(Bi_2Te_3)_{0.06}$ with proper annealing-quenching treatment can reach $\sim$0.8 at 300 K and $\sim$1.3 at 373 K, showing great promise for competing with the most famous Bi_2Te_3-based alloys. The quenched GeTe-based alloys obtain a sharp increase of μ_w owing to the greatly increased contribution of the light valence bands by multiple-band convergence, as a result of the combined tuning of α and Δ. A slight decrease of κ_{lat} can also be achieved in these quenched samples, which should be ascribed to the extra phase boundaries and enhanced anharmonicity. Thus, this work embodies a novel phase-engineering strategy to decouple the electron and phonon transport, simultaneously realizing the sharp increase of μ_w and the decrease of κ_{lat} for enhancing ZT, which also shows promise for other TE materials.

EXPERIMENTAL PROCEDURES

Resource availability

Lead contact
Further information and requests for resources and materials should be directed to and will be fulfilled by the lead contact, Chaohua Zhang (zhangch@szu.edu.cn).

Materials availability
The materials in this study will be made available on request.

Data and code availability
All data supporting the findings in this paper are presented in the article and supplemental information or are available from the corresponding author upon request.

Synthesis process
To prepare the samples of $(Ge_{0.87}Pb_{0.13}Te)_{0.94}(Bi_2Te_3)_{0.06}$, $(GeTe)_{0.93}(Bi_2Te_3)_{0.07}$, $(PbTe)_{0.93}(Bi_2Te_3)_{0.07}$, and $(SnTe)_{0.93}(Bi_2Te_3)_{0.07}$, the raw materials of bulk Ge (99.99%), Te (99.99%), Bi (99.99%), Pb (99.99%), and Sn (99.99%) were stoichiometrically weighted and then sealed in the evacuated quartz tube (5 × 10^{-3} Pa). The samples were slowly heated to 1,050°C, held for 20 h for the complete mixing and reaction, and were slowly cooled to 600°C. After holding at 600°C for 10 h, the

CellPress
OPEN ACCESS

Cell Reports
Physical Science
Article

samples were subsequently allowed to cool down to RT by liquid-nitrogen quenching (or in 4/10 h). The obtained alloys were milled into powders by an agate mortar and then were consolidated by SPS under axial pressure of 60 MPa at 600°C for 8 min. For the post-annealing treatment, those SPS-derived samples were sealed in the evacuated quartz tubes ($<5 \times 10^{-3}$ Pa) and were then heated up to the required temperatures (300°C, 400°C, 500°C, and 600°C) and held for 10 h. After that, the samples were cooled down to RT by liquid-nitrogen quenching.

Characterization methods

The electrical properties of σ and S were measured by the ZEM-3 instrument in a helium atmosphere (Ulvac-Riko, $\pm 5\%$ uncertainty). The κ was calculated using the equation $\kappa = \lambda C_p d$, where the thermal diffusivity λ was measured by a laser flash method (LFA 467, NETZSCH, $\pm 3\%$ uncertainty), the density d was measured by an Archimedes method, and the C_p was determined by the Dulong-Petit law. The DSC data were collected using an instrument of DSC 404F3 (NETZSCH) with a heating rate of 10 Kmin^{-1} from RT to 500°C. The Hall carrier concentration and mobility were measured by the Physical Properties Measurement Systems (PPMS, Quantum Design).

Raman spectra were acquired using a micro-Raman spectrometer (Horiba-LabRAM HR Evolution) with a ×50 objective lens (numerical aperture = 0.5) and a grating with 600 lines/nm and excitation energy of ∼2.33 eV. For the temperature-dependent Raman measurements, a heating chamber (CIA-RC102 FLOW CRYOSTATS) equipped with a temperature controller (Lakeshore) was employed. For each measurement, the liquid nitrogen and temperature controller were used to control the sample temperature, which was stabilized for 10 min before acquiring each spectrum. The XRD patterns were obtained using the Bruker D8 Advance SS/18 kW diffractometer with Cu Kα radiation operating at 40 kV × 200 mA, and the scanning rate was set at 5° per minute. The XRD Rietveld refinements were performed by the Topas 3.1 software. TEM characterization was carried out using the instruments of FEI Tecnai G2 F30 and JEM-F200. TEM samples were prepared by the standard mechanical grinding and followed by the ion-milling process. Limited by the facilities, liquid nitrogen was not used during the ion-milling process, which may erase metastable structures more or less.

DFT calculations

The Vienna Ab initio Simulation Package (VASP) was utilized for the DFT calculations.[53] The exchange and correlation interactions were represented by the fully relativistic Perdew-Burke-Ernzerhof (PBE) generalized gradient approximation functional.[54] The plane wave cutoff energy was set to 500 eV, atomic coordinates were relaxed until the total energy converged to 10^{-6} eV, and the spin-orbit-coupling effect was considered.

SUPPLEMENTAL INFORMATION

Supplemental information can be found online at https://doi.org/10.1016/j.xcrp.2022.101009.

**Cell Reports
Physical Science**
Article

CellPress
OPEN ACCESS

AUTHOR CONTRIBUTIONS

L.W. contributed to the sample preparations, characterizations of XRD and TEM, and writing and revising the manuscript. S.F. contributed to the Raman characterizations and corresponding writing; J.L., L.H., and F.L. contributed to the methodology and resources; W.X. contributed to the methodology and resource of Raman and writing – review & editing; T.M. contributed to writing – review & editing and validation; C.Z. led the project, provided supervision, conceptualization, methodology, DFT calculations, writing – review & editing, validation, and funding acquisition.

DECLARATION OF INTERESTS

The authors declare no competing interests.

REFERENCES

1. Snyder, G.J., and Toberer, E.S. (2008). Complex thermoelectric materials. Nat. Mater. 7, 105–114. https://doi.org/10.1038/nmat2090.

2. Zhu, T., Liu, Y., Fu, C., Heremans, J.P., Snyder, J.G., and Zhao, X. (2017). Compromise and synergy in high-efficiency thermoelectric materials. Adv. Mater. 29, 1605884. https://doi.org/10.1002/adma.201605884.

3. Chen, Z., Zhang, X., and Pei, Y. (2018). Manipulation of phonon transport in thermoelectrics. Adv. Mater. 30, 1705617. https://doi.org/10.1002/adma.201705617.

4. Lee, S., Hippalgaonkar, K., Yang, F., Hong, J., Ko, C., Suh, J., Liu, K., Wang, K., Urban, J.J., Zhang, X., et al. (2017). Anomalously low electronic thermal conductivity in metallic vanadium dioxide. Science 355, 371–374. https://doi.org/10.1126/science.aag0410.

5. Snyder, G.J., Snyder, A.H., Wood, M., Gurunathan, R., Snyder, B.H., and Niu, C. (2020). Weighted mobility. Adv. Mater. 32, 2001537. https://doi.org/10.1002/adma.202001537.

6. Li, J., Zhang, X., Chen, Z., Lin, S., Li, W., Shen, J., Witting, I.T., Faghaninia, A., Chen, Y., Jain, A., et al. (2018). Low-symmetry rhombohedral GeTe thermoelectrics. Joule 2, 976–987. https://doi.org/10.1016/j.joule.2018.02.016.

7. Li, A., Hu, C., He, B., Yao, M., Fu, C., Wang, Y., Zhao, X., Felser, C., and Zhu, T. (2021). Demonstration of valley anisotropy utilized to enhance the thermoelectric power factor. Nat. Commun. 12, 5408. https://doi.org/10.1038/s41467-021-25722-0.

8. Hong, M., Wang, Y., Feng, T., Sun, Q., Xu, S., Matsumura, S., Pantelides, S.T., Zou, J., and Chen, Z.G. (2019). Strong phonon-phonon interactions securing extraordinary thermoelectric Ge₁₋ₓSbₓTe with Zn-alloying-induced band alignment. J. Am. Chem. Soc. 141, 1742–1748. https://doi.org/10.1021/jacs.8b12624.

9. Liu, H., Zhang, X., Li, J., Bu, Z., Meng, X., Ang, R., and Li, W. (2019). Band and phonon engineering for thermoelectric enhancements of rhombohedral GeTe. ACS Appl. Mater. Interfaces 11, 30756–30762. https://doi.org/10.1021/acsami.9b07455.

10. Mori, T. (2017). Novel principles and nanostructuring methods for enhanced thermoelectrics. Small 13, 1702013. https://doi.org/10.1002/smll.201702013.

11. Wu, D., Xie, L., Xu, X., and He, J. (2019). High thermoelectric performance achieved in GeTe-Bi₂Te₃ pseudo-binary via van der Waals gap-induced hierarchical ferroelectric domain structure. Adv. Funct. Mater. 29, 1806613. https://doi.org/10.1002/adfm.201806613.

12. Xie, L., Chen, Y., Liu, R., Song, E., Xing, T., Deng, T., Song, Q., Liu, J., Zheng, R., Gao, X., et al. (2020). Stacking faults modulation for scattering optimization in GeTe-based thermoelectric materials. Nano Energy 68, 104347. https://doi.org/10.1016/j.nanoen.2019.104347.

13. Chen, L.C., Chen, P.Q., Li, W.J., Zhang, Q., Struzhkin, V.V., Goncharov, A.F., Ren, Z., and Chen, X.J. (2019). Enhancement of thermoelectric performance across the topological phase transition in dense lead selenide. Nat. Mater. 18, 1321–1326. https://doi.org/10.1038/s41563-019-0499-9.

14. Byeon, D., Sobota, R., Delime-Codrin, K., Choi, S., Hirata, K., Adachi, M., Kiyama, M., Matsuura, T., Yamamoto, Y., Matsunami, M., and Takeuchi, T. (2019). Discovery of colossal Seebeck effect in metallic Cu₂Se. Nat. Commun. 10, 72. https://doi.org/10.1038/s41467-018-07877-5.

15. Liu, H., Yuan, X., Lu, P., Shi, X., Xu, F., He, Y., Tang, Y., Bai, S., Zhang, W., Chen, L., et al. (2013). Ultrahigh thermoelectric performance by electron and phonon critical scattering in Cu₂Se₁₋ₓIₓ. Adv. Mater. 25, 6607–6612. https://doi.org/10.1002/adma.201302660.

16. Brown, D.R., Day, T., Borup, K.A., Christensen, S., Iversen, B.B., and Snyder, G.J. (2013). Phase transition enhanced thermoelectric figure-of-merit in copper chalcogenides. APL Mater. 1, 052107. https://doi.org/10.1063/1.4827595.

17. Agne, M.T., Lange, F.R., Male, J.P., Siegert, K.S., Volker, H., Poltorak, C., Poitz, A., Siegrist, T., Maier, S., Snyder, G.J., and Wuttig, M. (2021). Disorder-induced Anderson-like localization for bidimensional thermoelectrics optimization. Matter 4, 2970–2984. https://doi.org/10.1016/j.matt.2021.07.017.

18. Hong, M., Chen, Z., Yang, L., Zou, Y., Dargusch, M.S., Wang, H., and Zou, J. (2018). Realizing zT of 2.3 in Ge₁₋ₓ₋ySbₓInyTe via reducing the phase-transition temperature and introducing resonant energy doping. Adv. Mater. 30, 1705942. https://doi.org/10.1002/adma.201705942.

19. Tsai, Y.F., Wei, P.C., Chang, L., Wang, K.K., Yang, C.C., Lai, Y.C., Hsing, C.R., Wei, C.M., He, J., Snyder, G.J., and Wu, H.J. (2021). Compositional fluctuations locked by athermal transformation yielding high thermoelectric performance in GeTe. Adv. Mater. 33, 2005612. https://doi.org/10.1002/adma.202005612.

20. Li, J., Zhang, X., Wang, X., Bu, Z., Zheng, L., Zhou, B., Xiong, F., Chen, Y., and Pei, Y. (2018). High-performance GeTe thermoelectrics in both rhombohedral and cubic phases. J. Am. Chem. Soc. 140, 16190–16197. https://doi.org/10.1021/jacs.8b09147.

21. Chang, C., Wang, D., He, D., He, W., Zhu, F., Wang, G., He, J., and Zhao, L. (2019). Realizing high-ranged out-of-plane ZTs in n-type SnSe crystals through promoting continuous phase transition. Adv. Energy Mater. 9, 1901334. https://doi.org/10.1002/aenm.201901334.

22. Sun, S., Li, Y., Chen, Y., Xu, X., Kang, L., Zhou, J., Xia, W., Liu, S., Wang, M., Jiang, J., et al. (2020). Electronic origin of the enhanced thermoelectric efficiency of Cu₂Se. Sci. Bull. (Beijing). 65, 1888–1893. https://doi.org/10.1016/j.scib.2020.07.007.

23. Liang, Q., Yang, D., Xia, F., Bai, H., Peng, H., Yu, R., Yan, Y., He, D., Cao, S., Van Tendeloo, G., et al. (2021). Phase-transformation-induced giant deformation in thermoelectric Ag₂Se

semiconductor. Adv. Funct. Mater. *31*, 2106938. https://doi.org/10.1002/adfm.202106938.

24. Zhu, H., Zhao, T., Zhang, B., An, Z., Mao, S., Wang, G., Han, X., Lu, X., Zhang, J., and Zhou, X. (2020). Entropy engineered cubic n-Type AgBiSe$_2$ alloy with high thermoelectric performance in fully extended operating temperature range. Adv. Energy Mater. *11*, 2003304. https://doi.org/10.1002/aenm.202003304.

25. Agne, M.T., Voorhees, P.W., and Snyder, G.J. (2019). Phase transformation contributions to heat capacity and impact on thermal diffusivity, thermal conductivity, and thermoelectric performance. Adv. Mater. *31*, 1902980. https://doi.org/10.1002/adma.201902980.

26. Bai, G., Yu, Y., Wu, X., Li, J., Xie, Y., Hu, L., Liu, F., Wuttig, M., Cojocaru-Mirédin, O., and Zhang, C. (2021). Boron strengthened GeTe-based alloys for robust thermoelectric devices with high output power density. Adv. Energy Mater. *11*, 2102012. https://doi.org/10.1002/aenm.202102012.

27. Zhao, K., Zhu, C., Qiu, W., Yang, S., Su, H., Qiu, P., He, Y., Guan, M., Wei, T.R., Ma, J., et al. (2022). Novel meta-phase arising from large atomic size mismatch. Matter *5*, 605–615. https://doi.org/10.1016/j.matt.2021.12.003.

28. Zheng, Z., Su, X., Deng, R., Stoumpos, C., Xie, H., Liu, W., Yan, Y., Hao, S., Uher, C., Wolverton, C., et al. (2018). Rhombohedral to cubic conversion of GeTe via MnTe alloying leads to ultralow thermal conductivity, electronic band convergence, and high thermoelectric performance. J. Am. Chem. Soc. *140*, 2673–2686. https://doi.org/10.1021/jacs.7b13611.

29. Zhang, X., Bu, Z., Lin, S., Chen, Z., Li, W., and Pei, Y. (2020). GeTe thermoelectrics. Joule *4*, 986–1003. https://doi.org/10.1016/j.joule.2020.03.004.

30. Liu, Z., Sun, J., Mao, J., Zhu, H., Ren, W., Zhou, J., Wang, Z., Singh, D.J., Sui, J., Chu, C.W., and Ren, Z. (2018). Phase-transition temperature suppression to achieve cubic GeTe and high thermoelectric performance by Bi and Mn codoping. Proc. Natl. Acad. Sci. USA *115*, 5332–5337. https://doi.org/10.1073/pnas.1802020115.

31. Bu, Z., Chen, Z., Zhang, X., Lin, S., Mao, J., Li, W., Chen, Y., and Pei, Y. (2020). Near-room-temperature rhombohedral Ge$_{1-x}$Pb$_x$Te thermoelectrics. Mater. Today Phys. *15*, 100260. https://doi.org/10.1016/j.mtphys.2020.100260.

32. Perumal, S., Roychowdhury, S., Negi, D.S., Datta, R., and Biswas, K. (2015). High thermoelectric performance and enhanced mechanical stability of p-type Ge$_{1-x}$Sb$_x$Te. Chem. Mater. *27*, 7171–7178. https://doi.org/10.1021/acs.chemmater.5b03434.

33. Dong, J., Sun, F.-H., Tang, H., Pei, J., Zhuang, H.-L., Hu, H.-H., Zhang, B.-P., Pan, Y., and Li, J.-F. (2019). Medium-temperature thermoelectric GeTe: vacancy suppression and band structure engineering leading to high performance. Energy Environ. Sci. *12*, 1396–1403. https://doi.org/10.1039/c9ee00317g.

34. Liu, Z., Gao, W., Zhang, W., Sato, N., Guo, Q., and Mori, T. (2020). High power factor and enhanced thermoelectric performance in Sc and Bi codoped GeTe: insights into the hidden role of rhombohedral distortion degree. Adv. Energy Mater. *10*, 2002588. https://doi.org/10.1002/aenm.202002588.

35. Gao, W., Liu, Z., Zhang, W., Sato, N., Guo, Q., and Mori, T. (2021). Improved thermoelectric performance of GeTe via efficient yttrium doping. Appl. Phys. Lett. *118*, 033901. https://doi.org/10.1063/5.0038957.

36. Li, J., Xie, Y., Zhang, C., Ma, K., Liu, F., Ao, W., Li, Y., and Zhang, C. (2019). Stacking fault-induced minimized lattice thermal conductivity in the high-performance GeTe-based thermoelectric materials upon Bi$_2$Te$_3$ alloying. ACS Appl. Mater. Interfaces *11*, 20064–20072. https://doi.org/10.1021/acsami.9b04984.

37. Samanta, M., Roychowdhury, S., Ghatak, J., Perumal, S., and Biswas, K. (2017). Ultrahigh average thermoelectric figure of merit, low lattice thermal conductivity and enhanced microhardness in nanostructured (GeTe)$_x$(AgSbSe$_2$)$_{100-x}$. Chem. Eur. J. *23*, 7438–7443. https://doi.org/10.1002/chem.201701480.

38. Liu, M., Zhu, J., Cui, B., Guo, F., Liu, Z., Zhu, Y., Guo, M., Sun, Y., Zhang, Q., Zhang, Y., et al. (2022). High-performance lead-free cubic GeTe-based thermoelectric alloy. Cell Rep. Phys. Sci. *3*, 100902. https://doi.org/10.1016/j.xcrp.2022.100902.

39. Hong, M., Lyv, W., Li, M., Xu, S., Sun, Q., Zou, J., and Chen, Z.-G. (2020). Rashba effect maximizes thermoelectric performance of GeTe derivatives. Joule *4*, 2030–2043. https://doi.org/10.1016/j.joule.2020.07.021.

40. Wang, L., Li, J., Zhang, C., Ding, T., Xie, Y., Li, Y., et al. (2020). Discovery of low-temperature GeTe-based thermoelectric alloys with high performance competing with Bi$_2$Te$_3$. J. Mater. Chem. A *8*, 1660–1667. https://doi.org/10.1039/c9ta11901a.

41. Liu, Z., Sato, N., Guo, Q., Gao, W., and Mori, T. (2020). Shaping the role of germanium vacancies in germanium telluride: metastable cubic structure stabilization, band structure modification, and stable N-type conduction. NPG Asia Mater. *12*, 66. https://doi.org/10.1038/s41427-020-00247-y.

42. Rosenthal, T., Urban, P., Nimmrich, K., Schenk, L., de Boor, J., Stiewe, C., and Oeckler, O. (2014). Enhancing the thermoelectric properties of germanium antimony tellurides by substitution with selenium in compounds Ge$_n$Sb$_2$(Te$_{1-x}$Se$_x$)$_{n+3}$ ($0 \leq x \leq 0.5$; $n \geq 7$). Chem. Mater. *26*, 2567–2578. https://doi.org/10.1021/cm404115k.

43. Qiu, Y., Jin, Y., Wang, D., Guan, M., He, W., Peng, S., et al. (2019). Realizing high thermoelectric performance in GeTe through decreasing the phase transition temperature via entropy engineering. J. Mater. Chem. A *7*, 26393–26401. https://doi.org/10.1039/c9ta10963c.

44. Sist, M., Kasai, H., Hedegaard, E.M.J., and Iversen, B.B. (2018). Role of vacancies in the high-temperature pseudodisplacive phase transition in GeTe. Phys. Rev. B *97*, 094116. https://doi.org/10.1103/PhysRevB.97.094116.

45. Bellin, C., Pawbake, A., Paulatto, L., Béneut, K., Biscaras, J., Narayana, C., et al. (2020). Functional monochalcogenides: Raman evidence linking properties, structure, and metavalent bonding. Phys. Rev. Lett. *125*, 145301. https://doi.org/10.1103/PhysRevLett.125.145301.

46. Pawbake, A., Bellin, C., Paulatto, L., Béneut, K., Biscaras, J., Narayana, C., et al. (2019). Pressure-induced phase transitions in germanium telluride: Raman signatures of anharmonicity and oxidation. Phys. Rev. Lett. *122*, 145701. https://doi.org/10.1103/PhysRevLett.122.145701.

47. Wu, H., Zhang, Y., Ning, S., Zhao, L.-D., and Pennycook, S.J. (2019). Seeing atomic-scale structural origins and foreseeing new pathways to improved thermoelectric materials. Mater. Horiz. *6*, 1548–1570. https://doi.org/10.1039/c9mh00543a.

48. Wu, D., Zhao, L.D., Hao, S., Jiang, Q., Zheng, F., Doak, J.W., Wu, H., Chi, H., Gelbstein, Y., Uher, C., et al. (2014). Origin of the high performance in GeTe-based thermoelectric materials upon Bi$_2$Te$_3$ doping. J. Am. Chem. Soc. *136*, 11412–11419. https://doi.org/10.1021/ja504896a.

49. Bayikadi, K.S., Sankar, R., Wu, C.T., Xia, C., Chen, Y., Chen, L.-C., et al. (2019). Enhanced thermoelectric performance of GeTe through in situ microdomain and Ge-vacancy control. J. Mater. Chem. A *7*, 15181–15189. https://doi.org/10.1039/c9ta03503f.

50. Chang, C., and Zhao, L.-D. (2018). Anharmoncity and low thermal conductivity in thermoelectrics. Mater. Today Phys. *4*, 50–57. https://doi.org/10.1016/j.mtphys.2018.02.005.

51. Kooi, B.J., and Wuttig, M. (2020). Chalcogenides by design: functionality through metavalent bonding and confinement. Adv. Mater. *32*, 1908302. https://doi.org/10.1002/adma.201908302.

52. Raty, J.-Y., and Wuttig, M. (2020). The interplay between Peierls distortions and metavalent bonding in IV–VI compounds: comparing GeTe with related monochalcogenides. J. Phys. D Appl. Phys. *53*, 234002. https://doi.org/10.1088/1361-6463/ab7e66.

53. Kresse, G., and Furthmüller, J. (1996). Efficient iterative schemes for ab initio total-energy calculations using a plane-wave basis set. Phys. Rev. B *54*, 11169–11186. https://doi.org/10.1103/physrevb.54.11169.

54. Perdew, J.P., Burke, K., and Ernzerhof, M. (1996). Generalized gradient approximation made simple. Phys. Rev. Lett. *77*, 3865–3868. https://doi.org/10.1103/physrevlett.77.3865.